

# Mn-Doped Nano-Hydroxyapatites as Theranostic Agents with Tumor pH-Amplified MRI-Signal Capabilities for Guiding Photothermal Therapy

Chengyu Li, Ziyou Ding, Yingchao Han 

State Key Laboratory of Advanced Technology for Materials Synthesis and Processing, Biomedical Materials and Engineering Research Center of Hubei Province, Wuhan University of Technology, Wuhan, 430070, People's Republic of China

Correspondence: Yingchao Han, Email hanyingchao@whut.com

**Background:** The integration of diagnostic and therapeutic functions into a biosafe nanoplatform with intelligent response functions at the tumor microenvironment (TME) is a promising strategy for cancer therapy.

**Methods:** Mn-doped nano-hydroxyapatite (nHAPMn) nanoparticles were successfully prepared via a simple coprecipitation method for magnetic resonance imaging (MRI)-guided photothermal therapy. This study is the first to report on the use of Mn to render biodegradable hydroxyapatite suitable for MRI and effective photothermal therapy (PTT) simultaneously by regulating the pH of nHAPMn during the preparation process.

**Results:** Combined with near-infrared (NIR) laser irradiation, a photothermal conversion efficiency of 26% and effective photothermal lethality *in vitro* were achieved. Moreover, the degradation of nHAPMn led to the release of Mn ions and amplified the MRI signals in an acidic TME, which confirmed that nHAPMn had a good pH-responsive MRI capacity in solid tumors. In animal experiments, tumors in the nHAPMn5+NIR group completely abated after 14 days of treatment, with no significant recurrence during the experiment.

**Conclusion:** Therefore, nHAPMn is promising as a nanotheranostic agent and can be effective in clinical diagnosis and therapy for treating cancer.

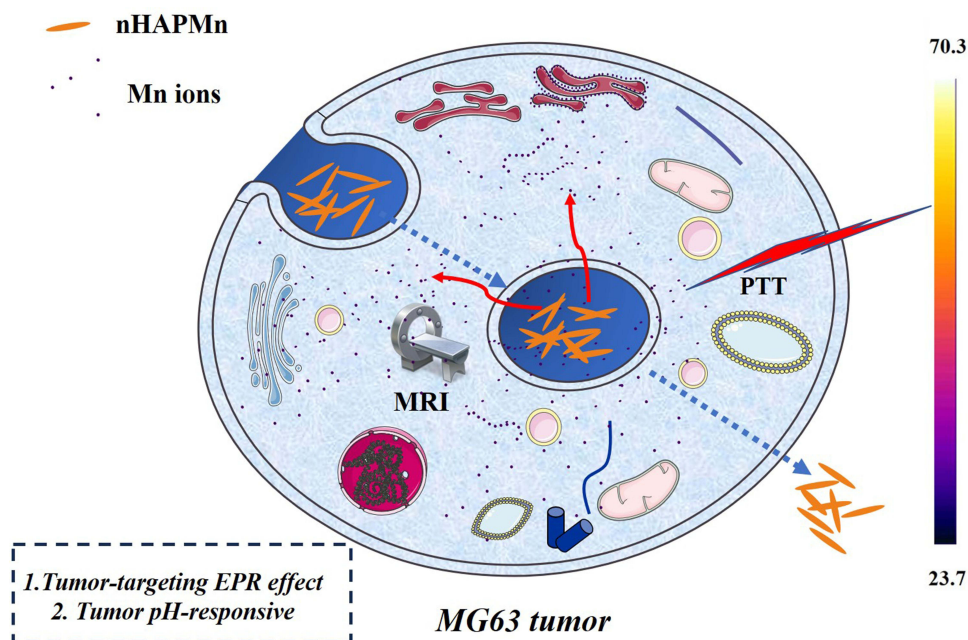
**Keywords:** photothermal therapy, magnetic resonance imaging, hydroxyapatite, manganese, pH-amplified

## Introduction

For decades, cancer has been considered a leading cause of death worldwide.<sup>1,2</sup> Recently, theranostic agents have gained increasing attention because they can identify the location and size of tumors, monitor treatment procedures in real time, and assess their effectiveness after treatment.<sup>3</sup> By combining the enhanced imaging capabilities of contrast agents with therapeutic agents, multiple dosing can be avoided, and the additional pressure on the body's blood clearance capacity can be significantly reduced, thereby improving the treatment efficiency.<sup>4</sup> For example, numerous studies have proven that Man-HA-MnO<sub>2</sub> NPs, MFMSNs, and HSA-MnO<sub>2</sub>-Ce6 NPs have an excellent therapeutic effect under the guidance of clinical diagnosis.<sup>5-8</sup>

Molecular imaging techniques, such as magnetic resonance imaging (MRI), positron emission tomography, X-ray computed tomography, and single photon emission computed tomography, play an important role in the clinical diagnosis of cancer.<sup>9</sup> Among them, MRI is a versatile imaging technique and has been widely used in cancer diagnosis owing to its high spatial resolution capacity, non-invasiveness, and unlimited depth of tissue penetration.<sup>6</sup> Many contrast agents are used in MRI, and they can be divided into T1 and T2 type preparations based on their mechanism of action. The former increases signal intensity on T1WI, whereas the latter decreases signal intensity on T2WI. Gd chelate is the most common MRI contrast agent for increasing signal intensity on T1WI.<sup>10</sup> However, it can increase the risk of renal systemic fibrosis or cause brain abnormalities in healthy patients.<sup>11</sup> Accordingly, many nanomaterials including iron oxide, manganese oxide, and other metal-based compounds have recently been considered for use in MRI because of their superior biosafety.<sup>6,12,13</sup> In addition,

## Graphical Abstract



traditional cancer treatments such as chemotherapy, radiotherapy (RT), and surgery are generally characterized by invasiveness, side effects, and low selectivity.<sup>8</sup> To solve these problems, many novel tumor treatment methods, such as photothermal therapy, chemodynamic therapy, and ultrasound therapy, have attracted considerable attention. Photothermal therapy (PTT), which uses near-infrared (NIR) light absorbers to convert light energy into heat energy to kill tumor cells, is considered as a promising treatment with high accuracy and low side effects.<sup>14–16</sup> In this context, the integration of MRI and photothermal therapy into a nanoplatform is expected to effectively improve the theranostic effect for treating cancer.

Mn is a transition metal that exists in more than five valence states, the most prevalent being  $Mn^{2+}$  and  $Mn^{4+}$ .<sup>17,18</sup> It can promote bone growth and development, protect the integrity of mitochondria in cells, maintain normal brain function, and improve the hematopoietic function of the body.<sup>19–21</sup> Recently, Mn-based contrast agents have attracted considerable attention as substitutes for Gd-based contrast agents used in MRI.<sup>22</sup> However, the non-biodegradable and potential long-term toxicity of current Mn-based contrast agents hinder the progress of clinical transformation in the future.<sup>23</sup> Endogenous biomaterials with natural biocompatibility and biodegradability are considered to be beneficial and can solve the biosafety problem in vivo; however, most endogenous biomaterials comprise inorganic structures, which need complex and time-consuming synthetic procedures to develop MRI contrast agents because of their poor contrast characteristics.<sup>3,24</sup> Thus, it is very important to explore endogenous materials with high contrast characteristics and facile synthetic procedures for clinical application. Nano-hydroxyapatite (nHAP) has attracted great interest as a bone substitute owing to its excellent biocompatibility and biodegradability.<sup>25,26</sup> In addition, various dopants can be easily doped into the crystal lattice of nHAP, which endows nHAP nanoparticles (NPs) with the optimal features required for medical applications, such as antibacterial properties, improved protein adsorption, and biological imaging capabilities.<sup>27,28</sup> Hence, Mn ion doping is expected to endow nHAP with properties that are essential for MRI applications and reduce the toxicity of Mn-based MRI contrast agents. In addition,  $Mn^{2+}$  can be oxidized by adjusting the pH conditions during the preparation of Mn-doped nHAP, leading to a higher absorbance in the NIR range and improving its photothermal performance.<sup>29</sup> However, to the best of the authors' knowledge, there are few reports on the use of Mn-based theranostic agents with an enhanced tumor microenvironment for MR imaging-guided photothermal therapy.

In this study, the biocompatible Mn-doped nHAP nanoparticles (nHAPMn NPs) were developed for MRI-guided photothermal therapy via a simple coprecipitation method (Figure 1). Owing to the enhanced permeability and retention

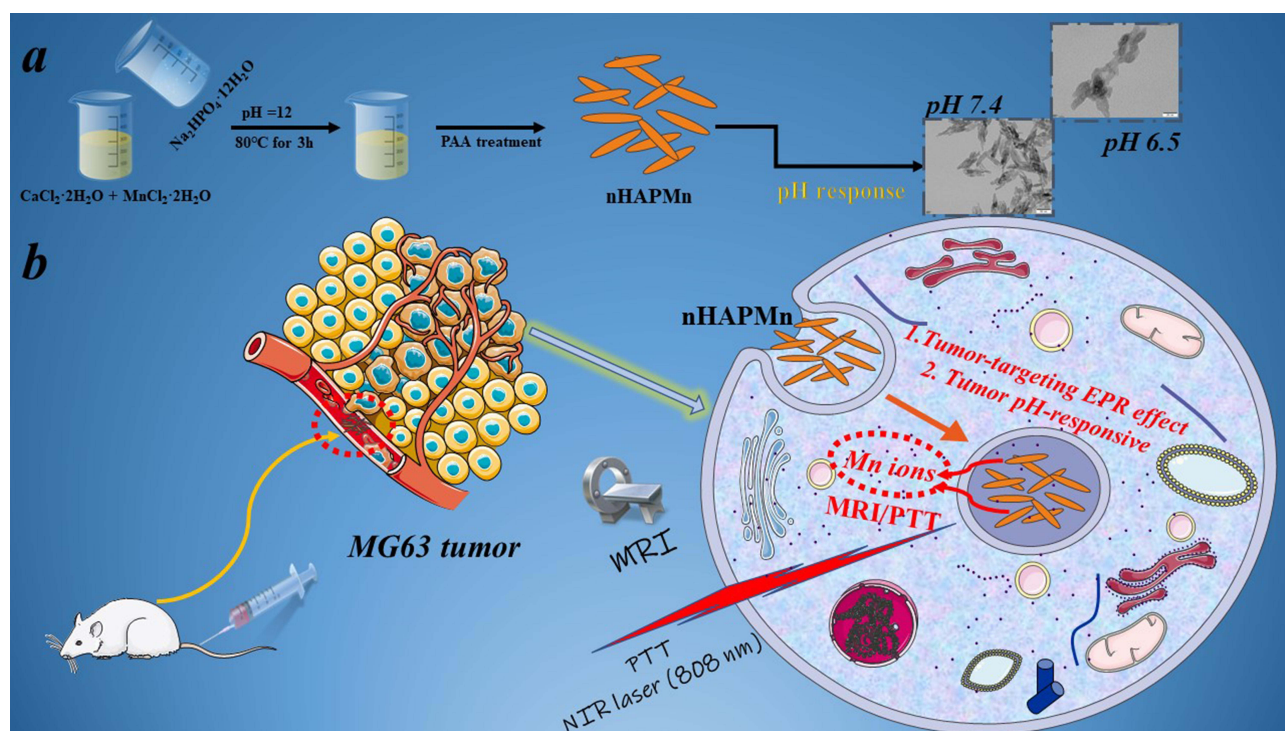


**Figure 1** (a and b) Schematic of nHAPMn NPs for MRI-guided photothermal therapy.

(EPR) effect, the nHAPMn system shows better relaxation and high accumulation in tumor, which improves its potential as an MRI contrast agent for cancer diagnosis. By regulating the pH in the reaction process, the NIR absorption capacity of the nHAPMn material can be considerably improved, which is beneficial for enhancing the photothermal ability to eliminate tumors. The tumor microenvironment (TME) characteristically displays mild acidity, which seriously hinders the therapeutic efficiency of the agent. Therefore, in this study, the pH values of different physiological environments were simulated, including normal body fluid (~7.4), TME (7.0–6.5), and endosome and lysosome (6.0–5.0). nHAPMn demonstrated improved Mn ion release capacity in a weakly acidic environment, possibly contributing to MRI-guided PTT performance.<sup>30</sup> These results demonstrate the potential of Mn-doped nHAP NPs as highly promising theranostic nanoagents for MR image-guided photothermal therapy.

## Experimental

### Materials

CaCl<sub>2</sub>·2H<sub>2</sub>O, MnCl<sub>2</sub>·2H<sub>2</sub>O, and Na<sub>2</sub>HPO<sub>4</sub>·12H<sub>2</sub>O were purchased from Sinopharm Chemical Reagent Beijing Co. Ltd. PAA (molecular weight = 1800), propidium iodide (PI), Cell counting kit-8 (CCK-8), and calcein acetoxymethyl ester (Calcein-AM) were purchased from Sigma-Aldrich. Deionized water (18.2 MΩ·cm resistivity at 25 °C) was used for all experiments, and all chemicals were used without further purification.

### Synthesis of Pure nHAP and nHAPMn

Pure and stoichiometric Mn ion-doped nHAP samples were prepared using a coprecipitation method. The molar ratio of (Ca+Mn)/P was 1.67, and the concentrations of the Mn ions relative to the overall molar content of (Ca+Mn) ions were 0, 1, 3, 5, and 10 mol%, denoted as nHAP, nHAPMn1, nHAPMn3, nHAPMn5, and nHAPMn10, respectively. To improve the stability of nHAPMn in solution, polyacrylic acid (PAA) was added to nHAPMn (the mass ratio of PAA/nHAPMn was 0.06) and subjected to ultrasonication for 10 min.

Taking the preparation of nHAPMn5 as an example: First, 7.14 mL CaCl<sub>2</sub>·2H<sub>2</sub>O solution (0.3 mol/L) was mixed with 1.125 mL MnCl<sub>2</sub>·2H<sub>2</sub>O solution (0.1 mol/L) and denoted as solution A. 7.5 mL Na<sub>2</sub>HPO<sub>4</sub>·12H<sub>2</sub>O solution (0.18 mol/L)

was prepared and denoted as solution B. Then, solution B was quickly poured into solution A with vigorous stirring, and the pH of the mixture was adjusted to 12 with NaOH. After 0.5 h of reaction, the mixture was heat treated at 80 °C for 3 h, separated by centrifugation, and washed four times. Finally, after incubation for 12 h at room temperature, the materials were resuspended in deionized water and 67.5 mg PAA was added for suspension. Furthermore, nHAPMn5 was respectively heat treated at different temperatures (25, 37, 80, 160, and 210 °C) for 3 h for magnetic measurements. nHAP was prepared without adding MnCl<sub>2</sub>·2H<sub>2</sub>O solution.

## Material Properties, in vitro and in vivo Experiments, and Statistical Analysis

The material properties, methods used for in vitro and in vivo experiments, and statistical analysis methods are introduced in the Supplementary experimental methods of supporting information.

All animal experiments were performed under the guidance of the Institutional Animal Care and Use Committee of the Wuhan University of Technology and in accordance with the policies of the National Ministry of Health. BALB/C mice were bought from Wuhan Center for Disease Control & Prevention, China and fed in Renmin Hospital of Wuhan University in accordance with the policies ethically and legally approved by the National Ministry of Health.

## Results and Discussion

Figure 2 shows that according to the standard data (JCPDS No.09-0432), the XRD pattern of nHAPMn has the characteristic diffraction peak of hexagonal nHAP, indicating a pure hydroxyapatite phase.<sup>31</sup> Compared with undoped nHAP, increasing the doping concentration of Mn (nHAPMn1-10) leads to a wider pattern. According to previous studies, this effect is attributed to the reduction in the crystal domain size caused by doping Mn ions as substitutes for Ca ions.<sup>32</sup> In addition, no discernible peaks corresponding to the second phase are observed. Table 1 lists the calculated parameters *a* and *c*, crystallite size, and crystallinity of pure nHAP and nHAPMn. When the Mn ion concentration increases, the cell parameter *c* and crystallite size decrease, indicating the incorporation of Mn ions into the nHAP

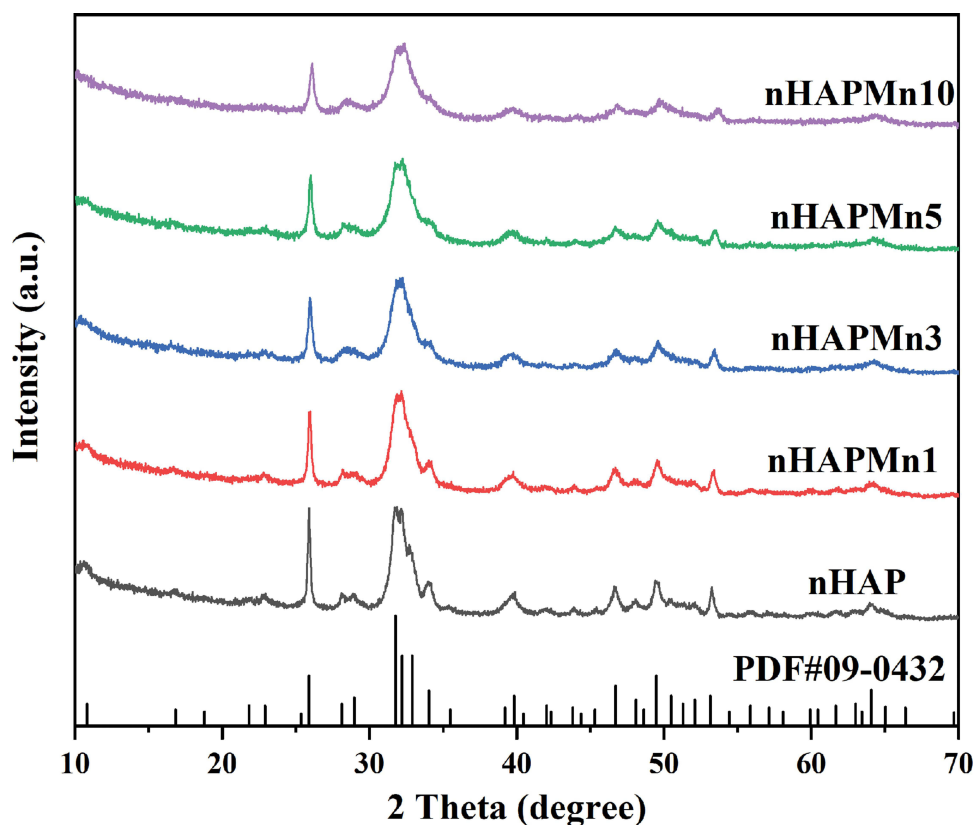


Figure 2 X-ray diffraction patterns of nHAP and nHAPMn.

**Table I** Lattice Parameters, Crystallite Sizes, and Crystallinity from XRD Analysis

Sample	a-Axis (Å)	c-Axis (Å)	Crystallite Size (Å)	Crystallinity (%)
nHAP	9.44248	6.87610	186	60.11
nHAPMn1	9.44077	6.86759	134	61.80
nHAPMn3	9.44241	6.85695	125	58.98
nHAPMn5	9.45590	6.85951	127	59.44
nHAPMn10	9.44581	6.82690	111	47.28

structure.<sup>21,33</sup> Replacing Mn with Ca leads to the contraction of lattice parameters and a reduction in grain size because the ion radius of Mn (+2 = 0.067 nm and +4 = 0.053 nm) is smaller than that of Ca (0.099 nm).<sup>34</sup> The compositions of the samples were determined using inductively coupled plasma atomic emission spectroscopy (ICP-AES) (Table S1), which indicated that the actual molar ratio of (Mn + Ca)/P decreases with increasing Mn ion concentration.

FE-SEM was used to investigate the effect of the substitution process on the morphologies of the pure and nHAPMn samples. As shown in Figures 3a–e, pure nHAP shows a nanorod morphology with a length of 50–200 nm, consistent with previous reports.<sup>35</sup> As the concentration of Mn ions increases, the nanorods become shorter. Previous XRD results

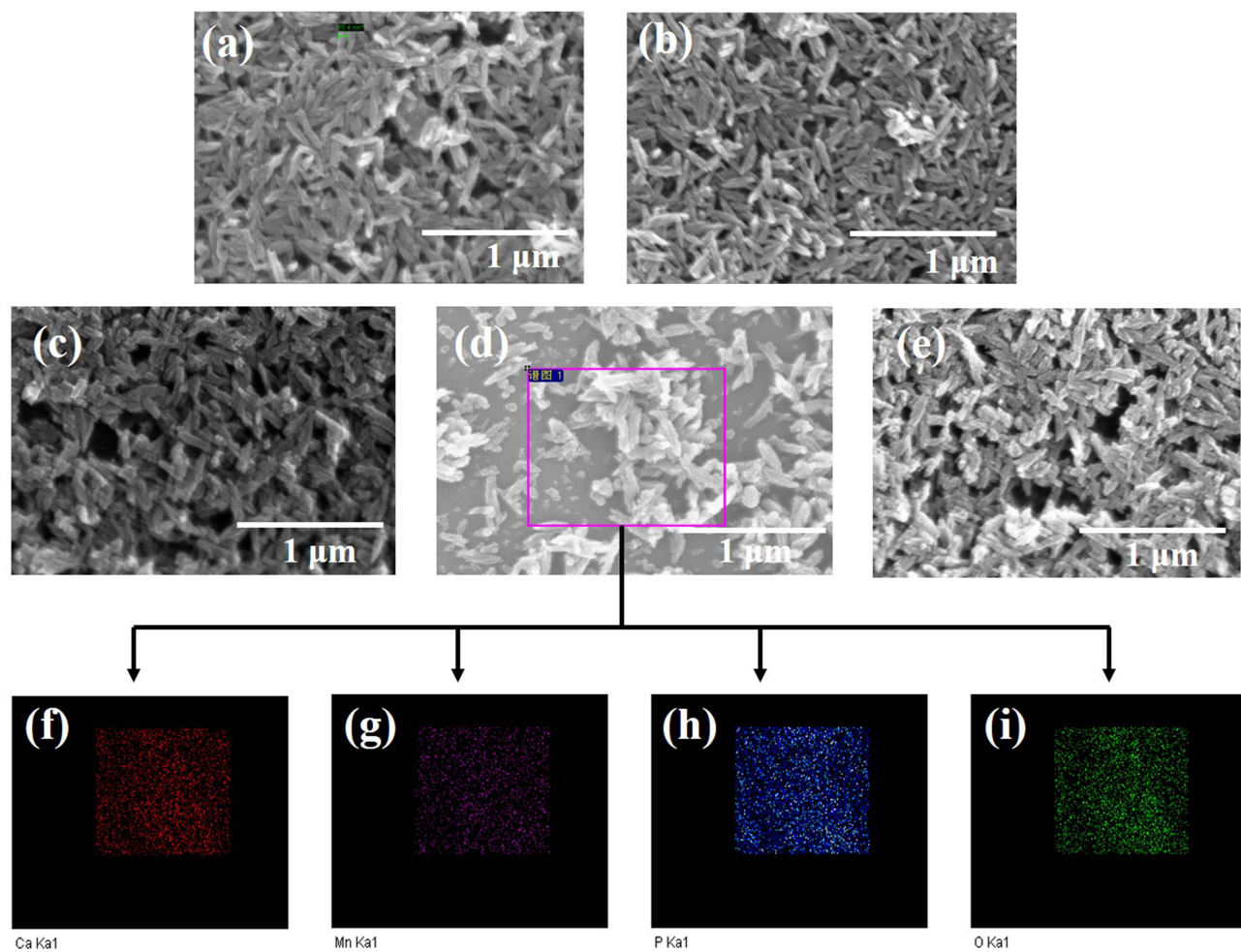


**Figure 3** Field emission scanning electron microscopy (FE-SEM) images of the (a) pure nHAP, (b) nHAPMn1, (c) nHAPMn3, (d) nHAPMn5, and (e) nHAPMn10 samples and (f–i) EDX mapping of nHAPMn5.

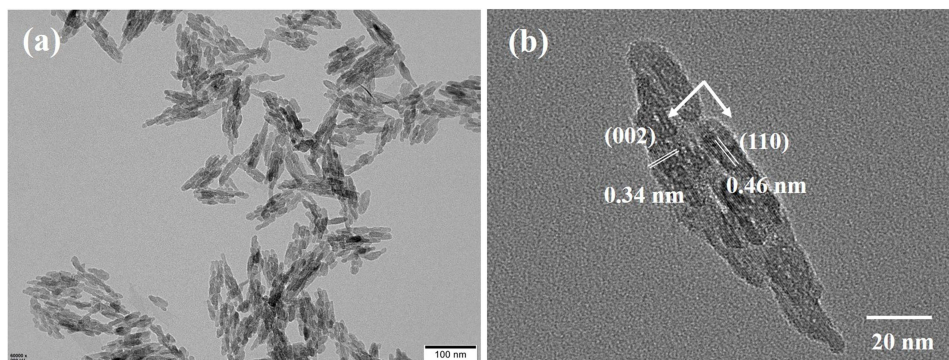
have shown that the crystallite size of the nHAPMn samples decreases as the concentration of Mn ions increases. Thus, the decrease in crystallite size results in a decrease in grain size. Figures 3f–i illustrate the elemental map distribution of nHAPMn5, indicating that the particles are homogeneously dispersed within the matrix and that Ca, P, O, and Mn are present in nHAPMn, which also confirms that the Mn ions have been doped successfully in the nHAP lattice.

HRTEM was performed to further investigate the interior morphology and size of the nHAPMn NPs. Figure 4 shows that the lattice fringes of nHAPMn5 are 0.34 and 0.46 nm, which are consistent with the (002) and (110) lattice planes in the hexagonal nHAP structure, respectively. Biodegradation is also an essential element for biomedical applications of nanomaterials; therefore, the biodegradation behavior of nHAPMn5 NPs in PBS solutions with different pH values was studied to simulate different physiological environments, including normal body fluids (~7.4), TME (7.0–6.5), and endosomes and lysosomes (6.0–5.0). As shown in Figure S1, the surface of nHAPMn5 is etched, and the boundary is blurred after 3 days of PBS treatment (pH 6.5). One possible reason for this phenomenon is that the nHAPMn5 particles are degraded in acidic solutions, and the released Mn ions increase the ionic strength of the solution and enhance the bridging effect between particles, which leads to the aggregation of the remaining nHAPMn5 particles.<sup>36,37</sup> In addition, we studied the degradation of nHAPMn5 NPs in PBS at different pH values (7.4, 6.5, and 5.5) by monitoring the release of Mn ions (Figure S2). The ICP results indicate that acidic conditions (pH 6.5, 5.5) facilitate Mn ion leakage from nHAPMn NPs, confirming that nHAPMn has an excellent pH-responsive capacity.

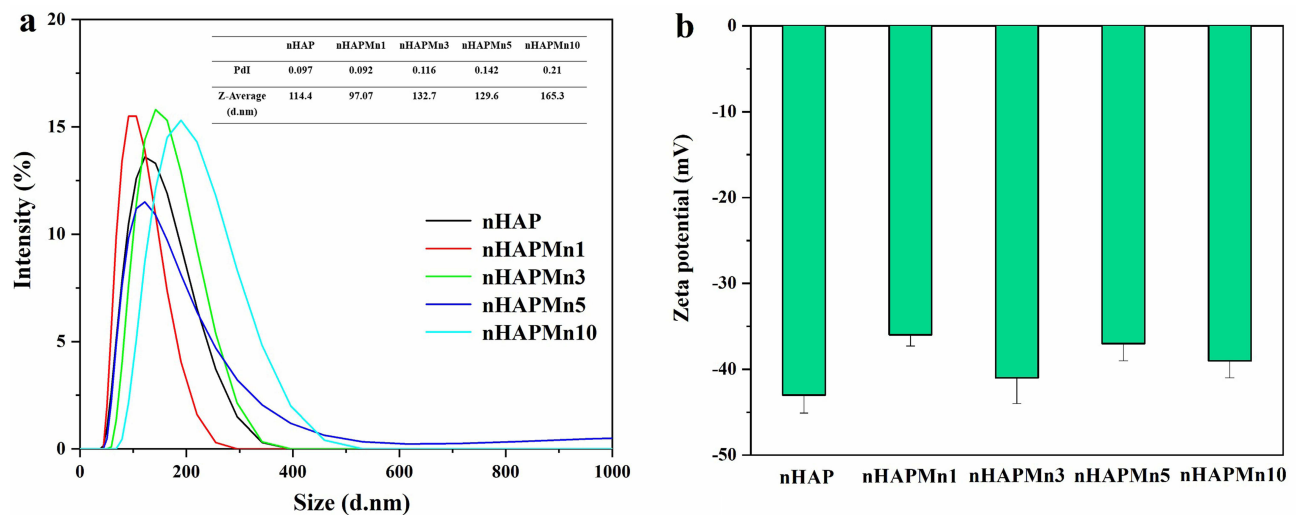
Previous studies have reported that particle size, dispersion, and surface chemical properties are important and significantly impact biological applications. Unfortunately, previously reported nHAP NPs easily accumulate and precipitate in aqueous solutions.<sup>38,39</sup> Therefore, the surface modification of nHAP to obtain a stable dispersive suspension system is a prerequisite for its biological application. PAA is a water-soluble polymer that can adjust its particle morphology by electrostatic interactions between the functional groups and the particle surface.<sup>40</sup> Moreover, the large number of carboxyl functional groups in PAA provides a hydrophilic surface for obtaining NPs with excellent water solubility and biological activity. Hence, PAA treatment was performed before measuring the particle size distribution of the samples. As shown in Figure S3, after PAA treatment, nHAPMn remains stable for a long time in aqueous solutions. However, in the absence of PAA, nHAPMn5 can quickly aggregate within 1 h. Figure 5a shows that the hydrodynamic diameter (HD) of nHAP and nHAPMn is approximately 100–200 nm, enabling effective uptake by tumor cells based on the EPR effect.<sup>7</sup> In addition, owing to the adequate number of carboxyl groups in PAA, nHAP and nHAPMn NPs have negatively charged surfaces (Figure 5b).

Figure 6 shows FT-IR spectra of the dried powders (nHAP and nHAPMn), exhibiting the typical vibrational modes of nHAP, indicating that incorporating Mn into nHAP does not influence the vibrational modes of pure nHAP.<sup>41,42</sup> The peaks between 560 and 630  $\text{cm}^{-1}$  and at 466  $\text{cm}^{-1}$  correspond to  $\nu_4 \text{PO}_4^{3-}$  and  $\nu_2 \text{PO}_4^{3-}$ , respectively.<sup>43,44</sup> No peaks corresponding to the functional groups of undoped nHAP were observed, indicating that nHAPMns obtained by coprecipitation synthesis maintain a similar structure to undoped nHAP.

Figure 7 shows the XPS spectra of the nHAPMn5 sample; the observed binding energies for Ca, P, O, and C are 347.05, 133.36, 531.27, and 285.31 eV, respectively. As is known, the color of the divalent Mn ions is pink, and it is relatively stable



**Figure 4** Transmission electron microscopy (TEM) (a) and high-resolution (HR) TEM (b) images of nHAPMn5.



**Figure 5** Dynamic light scattering (a) and zeta potentials (b) of nHAP and nHAPMn.

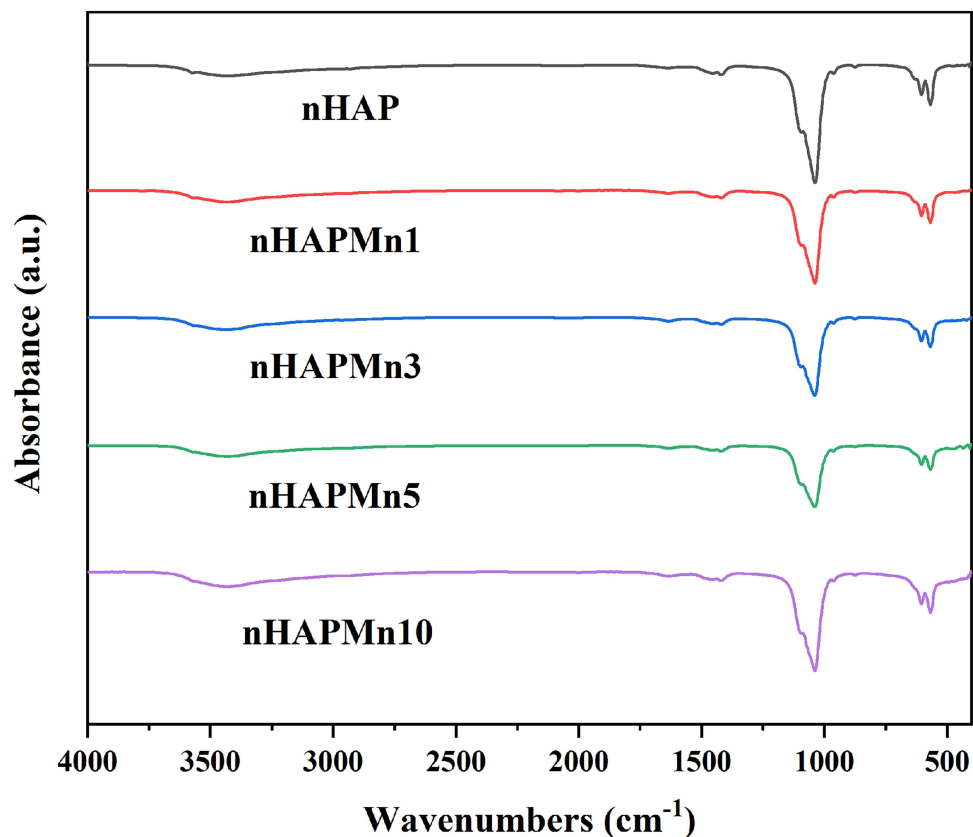


**Figure 6** Fourier transform infrared (FT-IR) spectra of nHAP and nHAPMn.

under slightly acidic conditions without an oxidant.<sup>45</sup> However, when exposed to strong oxidants such as potassium permanganate, it is oxidized to insoluble hydrate precipitates with valences of  $4^+$  (such as Mn oxyhydroxide, brown). Moreover, it can be easily oxidized by air or hydrogen peroxide under alkaline conditions or by reacting with silver ions or silver ammonia solutions.<sup>29</sup> Previous studies have shown that  $Mn^{2+}$  in doped materials mainly oxidizes to  $Mn^{4+}$ .<sup>11,46,47</sup> Therefore, the XPS data of Mn 2p were carefully peak fitted and are presented in the inset of Figure 7. The results show that  $Mn^{2+}$  and  $Mn^{4+}$  exist simultaneously, and the proportions of  $Mn^{2+}$  and  $Mn^{4+}$  are 42.77% and 57.23%, respectively.

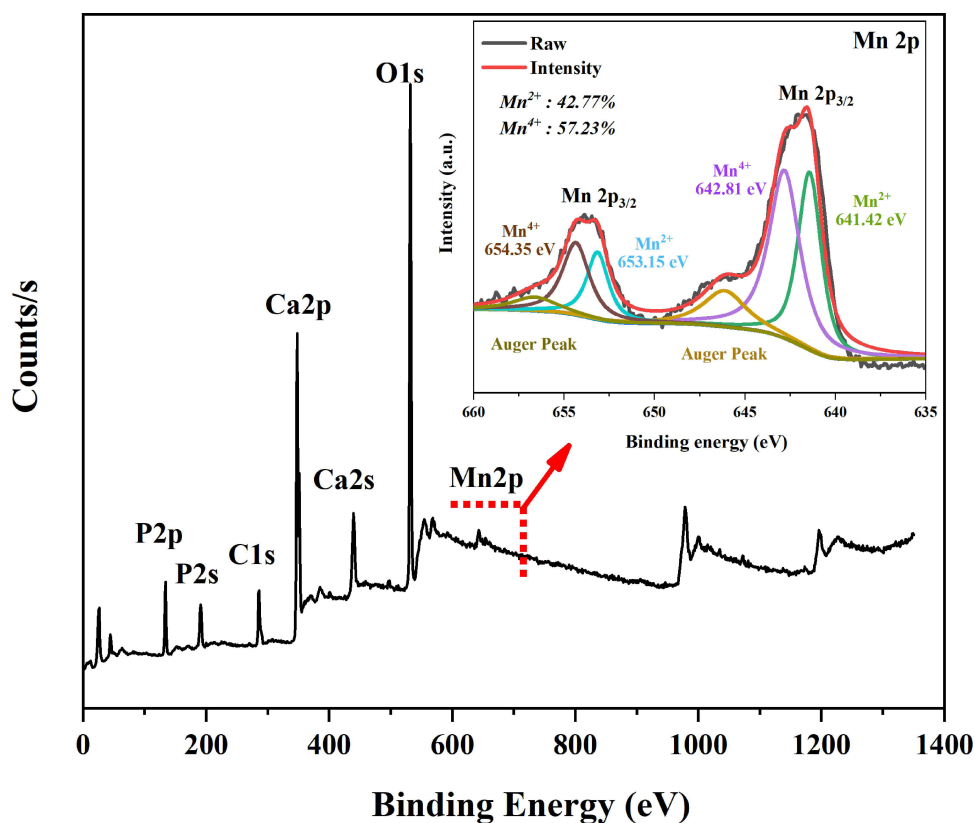


**Figure 7** X-ray photoelectron spectroscopy (XPS) survey scan and theoretical calculation of nHAPMn5.

Notably, during the preparation process, the color of the mixed solution of the nHAPMn ions rapidly turns dark brown at pH 12. Such a result is ascribed to a change in the valence state of the Mn ions from  $2^+$  to a  $2^+/4^+$  mixed valence state caused by the inference of the XPS test. Furthermore, the color of the nHAPMn solution becomes darker upon an increase in the Mn ion concentration, affecting the absorption of light (Figure S4). Hence, combining UV–vis–NIR absorption spectra and XPS analysis, we can conclude that the ratio between  $Mn^{2+}$  and  $Mn^{4+}$  in our study may be controlled by adjusting the pH during preparation. As shown in the UV–vis absorption spectrum of nHAPMn (Figure 8), upon increasing the Mn ion concentration, the spectrum shows a steady increase and higher absorbance in the NIR range. The strong absorption of nHAPMn NPs in the NIR range was expected to demonstrate better photothermal performance compared to pure nHAP. Therefore, the changes in the photothermal performance of nHAPMn after oxidation were further explored and are discussed in the following sections.

To evaluate the potential of nHAPMn as an MRI contrast agent, vibrating sample magnetometry (VSM) was used to quantify the magnetic field dependence. First, we studied VSM at different preparation temperatures (Figure S5). The results show that both coercivity and remanence are zero at room temperature. No hysteresis or magnetic transition were observed, indicating that all samples are paramagnetic, and the preparation temperature has no effect on the magnetization of the materials. Figure 9 shows the room-temperature magnetization curves of pure nHAP and nHAPMn at different Mn doping concentrations. The nHAPMn10 sample exhibited the highest magnetization value (0.34 emu/g), and the magnetization level of nHAP increased with increasing Mn doping concentrations, which is consistent with previous reports.<sup>47,48</sup> In addition, nHAPMn5 prepared at pH=12 showed relatively weak magnetization compared to that prepared at pH=10; however, the underlying mechanism is still unclear (Figure S6).

To further explore the potential of nHAPMn5 as a T1 MRI contrast agent, the longitudinal relaxation rate ( $r_1$ ) reflecting the ability to shorten the longitudinal relaxation time of water proton T1 was measured using a 7T MRI scanner at room temperature. The final values were calculated from the slopes of the curves presented in Figure 10. Increasing the doping concentration of Mn ions significantly enhances the MRI signal, indicating that NPs produce a high magnetic field gradient on

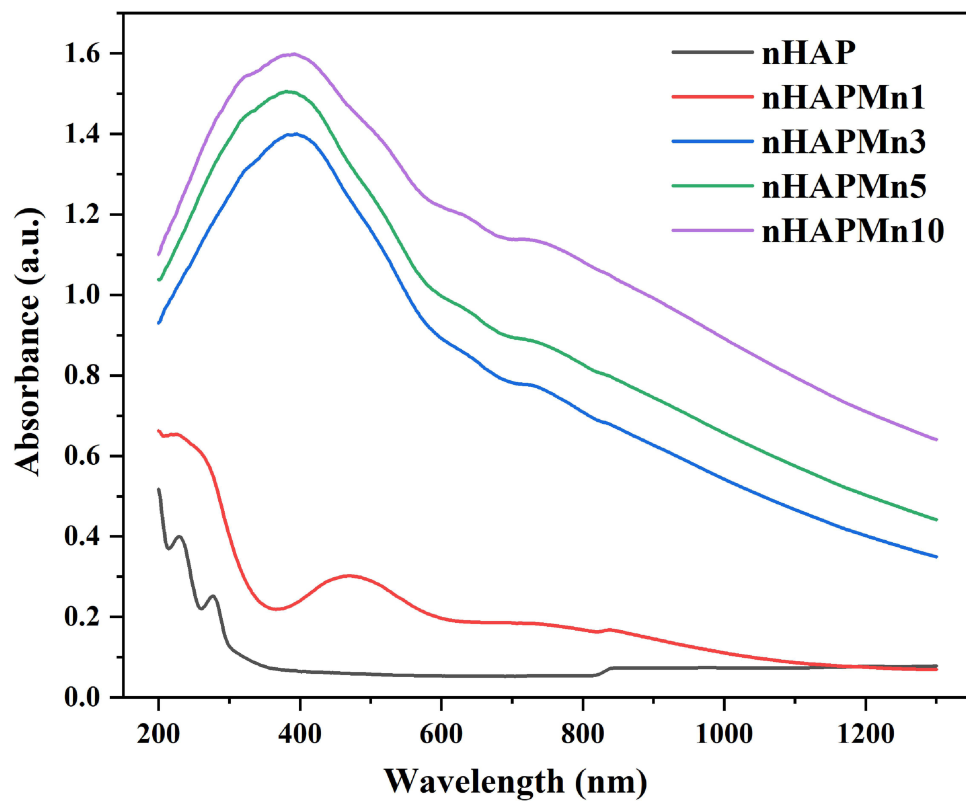


Figure 8 Ultraviolet-visible-NIR (UV-vis-NIR) absorption spectra of nHAP and nHAPMn.

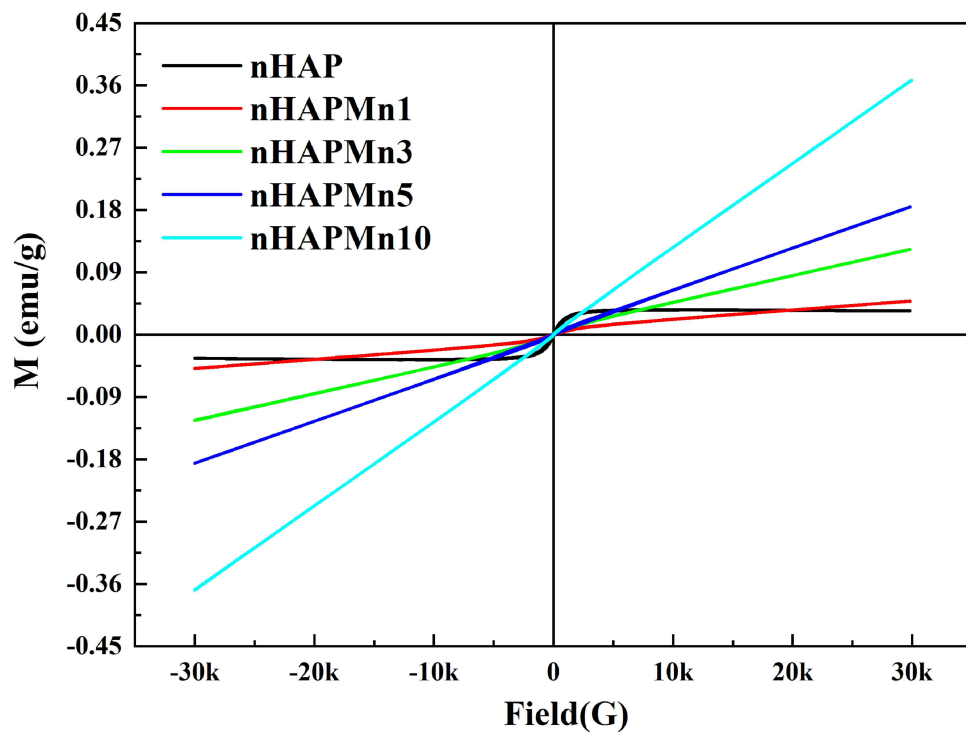
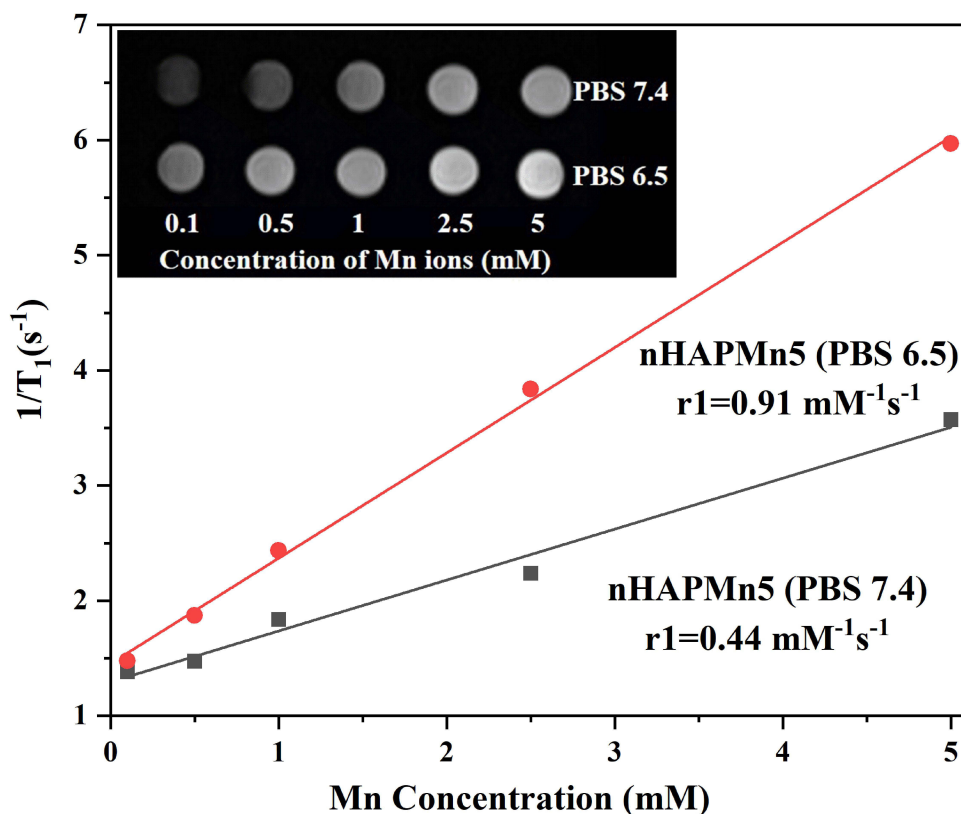


Figure 9 Magnetization curves of nHAP and nHAPMn powders measured at room temperature.



**Figure 10** In vitro MRI studies of nHAPMn5 treated with PBS (pH 6.5 and 7.4). Inset: T1-weighted MR images of nHAPMn5 at various Mn ions concentrations (0, 0.25, 0.5, 1.5, and 2.5 mM) and different PBS conditions (pH 6.5 and 7.4).

their surfaces. The  $r_1$  value of nHAPMn5 treated in normal conditions (PBS, pH 7.4) was  $0.44 \text{ mM}^{-1} \text{ s}^{-1}$ . After 24 h incubation in PBS (pH 6.5), the  $r_1$  value of nHAPMn5 was as high as  $0.91 \text{ mM}^{-1} \text{ s}^{-1}$ , which was twice as much as the former. Therefore, compared to a neutral environment, more Mn ions that enable facile exchange with the surrounding water molecules are produced in weakly acidic conditions, decreasing the relaxation times of the protons and resulting in more effective MRI enhancement. This indicates that nHAPMn5 could be a potential contrast agent for T1-weighted MRI in an acidic tumor microenvironment.

The photothermal performance was first investigated by recording the temperature changes of nHAPMn5 prepared at pH 10 and 12 (Figure S7). The results show that the photothermal performance of nHAPMn5 prepared at pH 12 is markedly improved compared to that at pH 10. Hence, the photothermal performance of nHAPMn5 prepared at pH 12 was further investigated. First, nHAP, nHAPMn1, nHAPMn3, and nHAPMn2 were respectively exposed to an 808 nm laser with a power density of  $1 \text{ W/cm}^2$  for 15 min. As shown in Figure 11a, under continuous NIR irradiation, the temperature of the nHAPMn NP sample increased rapidly. After irradiation for 15 min, nHAPMn NPs showed a significant temperature increase, but no significant temperature increase was detected in the nHAP samples. The temperature rise of nHAPMn is related to the increase in the Mn ion doping concentration. The corresponding infrared thermal images were obtained to monitor the photothermal effect of nHAPMn NPs (Figure 11b). In addition, with the increase in power density, the temperature increase is also significant (Figure 11c). Therefore, it can be concluded that nHAPMn NPs exhibits photothermal behavior that is dependent on the Mn ion doping concentration, laser power, and irradiation time. The efficiency of photothermal conversion is 26%, which was evaluated according to previous reports and the obtained data (Figure 11d).<sup>49</sup> In addition, the temperature profiles of nHAPMn5 upon light irradiation show no obvious changes during five repeated laser on and off cycles (Figure 11e), indicating its excellent photostability. Notably, the degradation ability is reported to be closely associated with the photothermal performance. Interestingly, the photothermal performance of nHAPMn5 soaked in PBS solutions with pH 5.5 and 6.5 for 7 days did not change

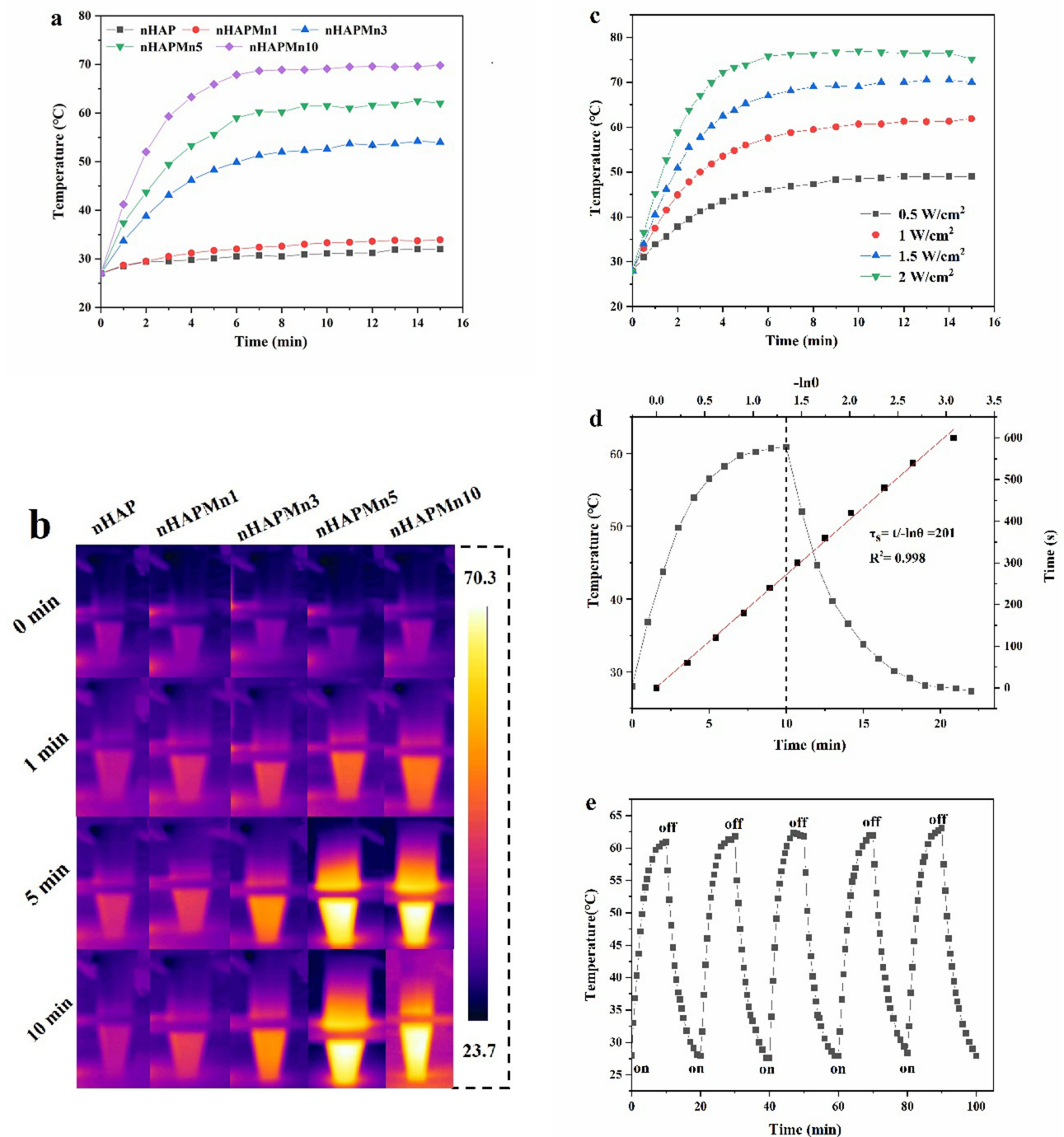


**Figure 11** (a) Heating properties of the nHAPMn solution with various Mn ion doping concentrations during irradiation with an 808 nm laser (1 W/cm<sup>2</sup>), (b) corresponding infrared thermal images of the nHAPMn solution with various Mn ion doping concentrations during irradiation with an 808 nm laser (1 W/cm<sup>2</sup>), (c) temperature increase of the nHAPMn5 solution irradiated with various power densities using an 808 nm laser, (d) corresponding heating and cooling curves and fitted line based on the data in the cooling stage, (e) thermal stability of nHAPMn5 during five on and off cycling processes.

significantly compared with that in a pH 7.4 PBS solution, indicating that the acidic environment does not affect the photothermal properties of the nHAPMn NPs (Figure S8). In summary, the obtained nHAPMn NPs are promising photothermal agents for tumor treatment.

CCK-8 and hemocompatibility assays were conducted to evaluate the biocompatibility of the prepared nHAPMn NPs before in vivo application. Figure 12a shows that no evident cell toxicity occurs after 1–3 days of incubation with the

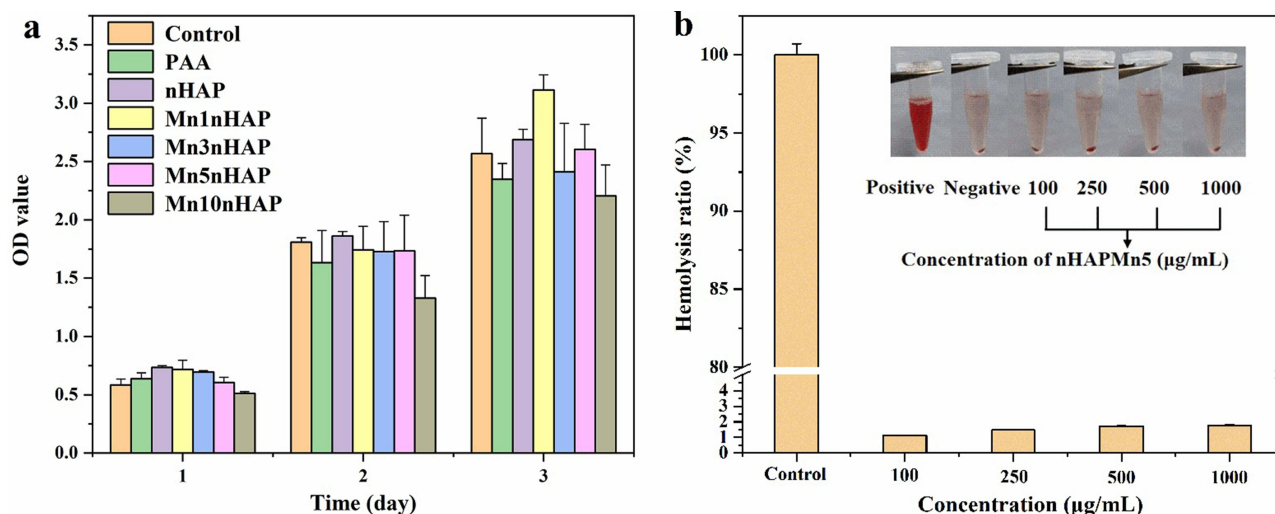


**Figure 12** (a) CCK-8 assay of MC3T3-E1 cells after incubation with nHAP and nHAPMn (100 µg/mL) after 1, 2, and 3 days of treatment. (b) Hemolysis of nHAPMn5 NPs after incubation with red blood cells at various concentrations.

nHAP and nHAPMn samples. Moreover, the pure PAA group exhibits no obvious cell toxicity, suggesting that PAA is not harmful to the human body. In addition, the calculated hemolysis ratio (Figure 12b) is less than 3% at the maximum nHAPMn5 concentration (1000 µg/mL). This finding indicates that nHAPMn NPs are biocompatible and can be used for in vivo cancer treatment by intravenous injection, which is attributed to the biocompatible synthetic route and excellent water stability.

MG63 cells were used to evaluate the PTT effect of nHAPMn NPs in vitro. As shown in Figure 13a, after being exposed to an 808 nm laser for 10 min, the relative viability of the MG63 cells decreased significantly upon an increase in the nHAPMn5 NP concentration. On the contrary, there was no significant difference in cell viability between groups without laser irradiation. Finally, approximately 87% of MG63 cells were killed by the PTT effect induced by nHAPMn5 (500 µg/mL). To further prove the thermal ablation effect of nHAPMn5 in vitro, a staining experiment was conducted using calcein-AM/PI to detect MG63 cell death induced by the PTT effect. As shown in Figure 13b, strong green

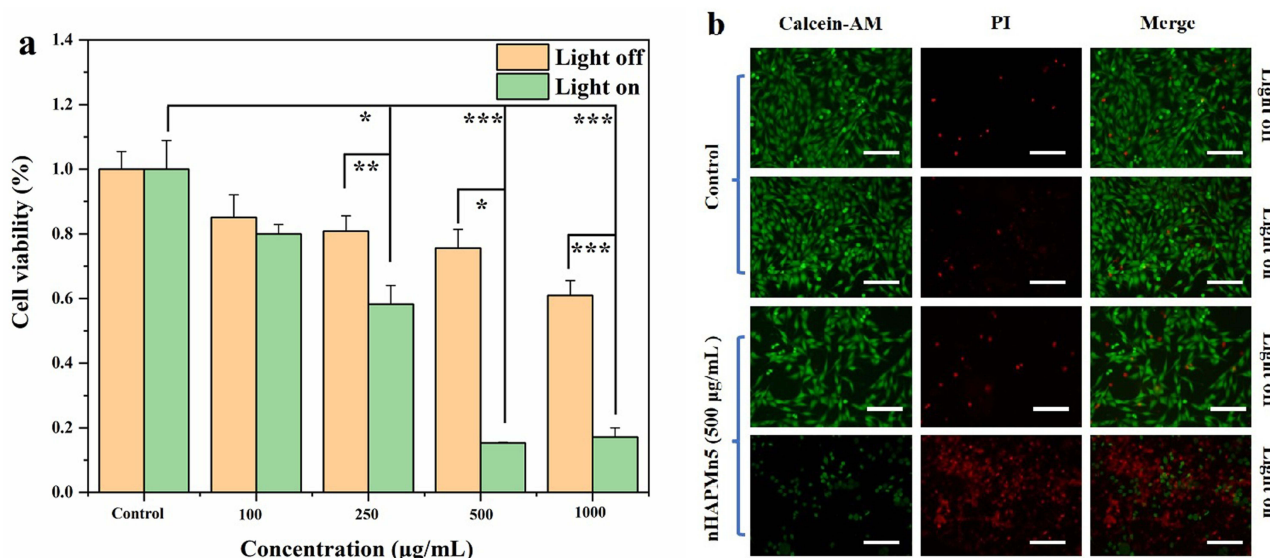


**Figure 13** (a) Cell viability of the MG63 cells treated with nHAPMn5 at different concentrations under an 808 nm laser (1 W/cm<sup>2</sup>) (\*P<0.05, \*\*P<0.01, \*\*\*P<0.001) and (b) corresponding fluorescence images of the MG63 cells stained with Calcein-AM and PI. Scale bar = 50 µm.

fluorescence was detected in the control (light off) and nHAPMn5 groups, indicating that most cells were alive.<sup>50,51</sup> However, strong red fluorescence signals were observed in the nHAPMn5 plus laser irradiation group, which indicated that local hyperthermia induced by nHAPMn5 led to high cell mortality. Based on these findings, it is inferred that nHAPMn5 exhibits good PTT response behavior and antitumor effect *in vitro*.<sup>52</sup>

Next, the *in vivo* performance of nHAPMn was evaluated in tumor-bearing mice using a 9.4T clinical MRI equipment. nHAPMn5 (1 mg per mouse) was injected intravenously into mice, and axial T1-weighted MR images were acquired at designed time intervals (0, 2, 4, 8, 12, and 24 h). As shown in the Figure 14a, 2 h after the injection of the sample, an enhanced signal and significant positive contrast effect were obtained in the tumor area, which indicated that a considerable number of nHAPMn5 NPs accumulated according to the EPR effect. After 24 h, the MR signal of the tumor area slightly weakened, but it could still be clearly detected. To better understand the change in the MR signal at the tumor area, ImageJ was used to quantitatively analyze the estimated corresponding signal intensity of the tumor and the results was shown in Figure 14b. Overall, before injection, the tumor exhibited a low signal intensity of 2.84 units; after intravenous injection of the substance, the signal intensity gradually increased reaching the highest level after 12 h and then slightly weakened, which was consistent with the MRI results. These results showed that nHAPMn has excellent contrast effects and high tumor targeting abilities.

Motivated by its excellent *in vitro* PTT anticancer and MR performance, we investigated the tumor inhibition capacity of nHAPMn5 in MG63 tumor-bearing mice. The mice bearing MG63 tumors were randomly divided into four groups: (i) PBS, (ii) PBS+NIR, (iii) nHAPMn5, and (iv) nHAPMn5+NIR. Based on the MRI results indicating that the highest concentration of nHAPMn5 in the tumor site appeared 12 h after injection, the PBS+NIR and nHAPMn5+NIR groups were arranged to receive 10 min NIR laser irradiation 12 h after injection. At the beginning of the treatment, nHAPMn5 (1 mg per mouse or equivalent PBS) was injected intravenously into the mice, and a thermal imaging camera was used to monitor the temperature changes in tumors in the PBS+NIR and nHAPMn5+NIR groups. Figure 15a shows that 12 h after injection of nHAPMn5, the temperature of the tumor rapidly reached approximately 50 °C under the irradiation of an 808 nm laser (1 W/cm<sup>2</sup>). On the contrary, under the same conditions, there was no obvious change in the PBS+NIR group, indicating the PTT ability of nHAPMn5 to tumors. After 10 min of PTT treatment, the tumor dimensions and body weights were recorded every 2 days. As shown in Figures 15b and c, the tumors in the nHAPMn5 + NIR groups were completely ablated after 14 days of treatment with no obvious recurrence during the experiments, suggesting the prominent PTT performance of nHAPMn. However, no tumor inhibitory effect was shown during the 14 day treatment in other groups. In addition, the body weight of mice remained stable during the treatment (Figure 15d), which indicated that nHAPMn exhibits good biocompatibility.<sup>53</sup> Hematoxylin-eosin (H&E) staining of tumor tissue (Figure 15e) showed a large area of apoptosis in the tumor treated with nHAPMn5 and 808 nm laser irradiation, whereas tumors treated with

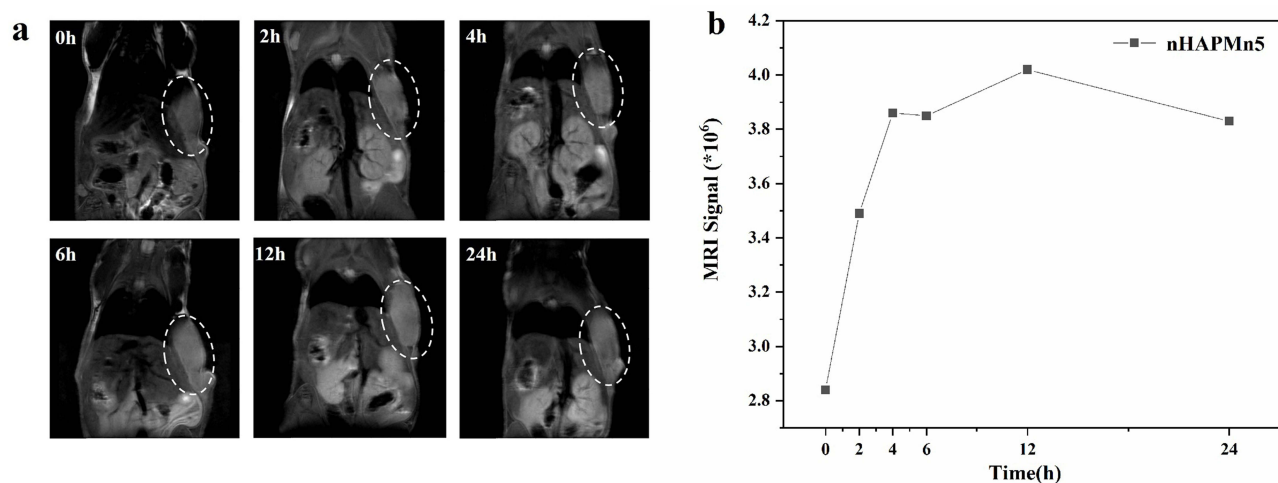


**Figure 14** (a) T1-weighted MR coronal images of tumor-bearing mice at different times after intravenous injection of nHAPMn5 and (b) corresponding T1-weighted MRI-signal intensities.

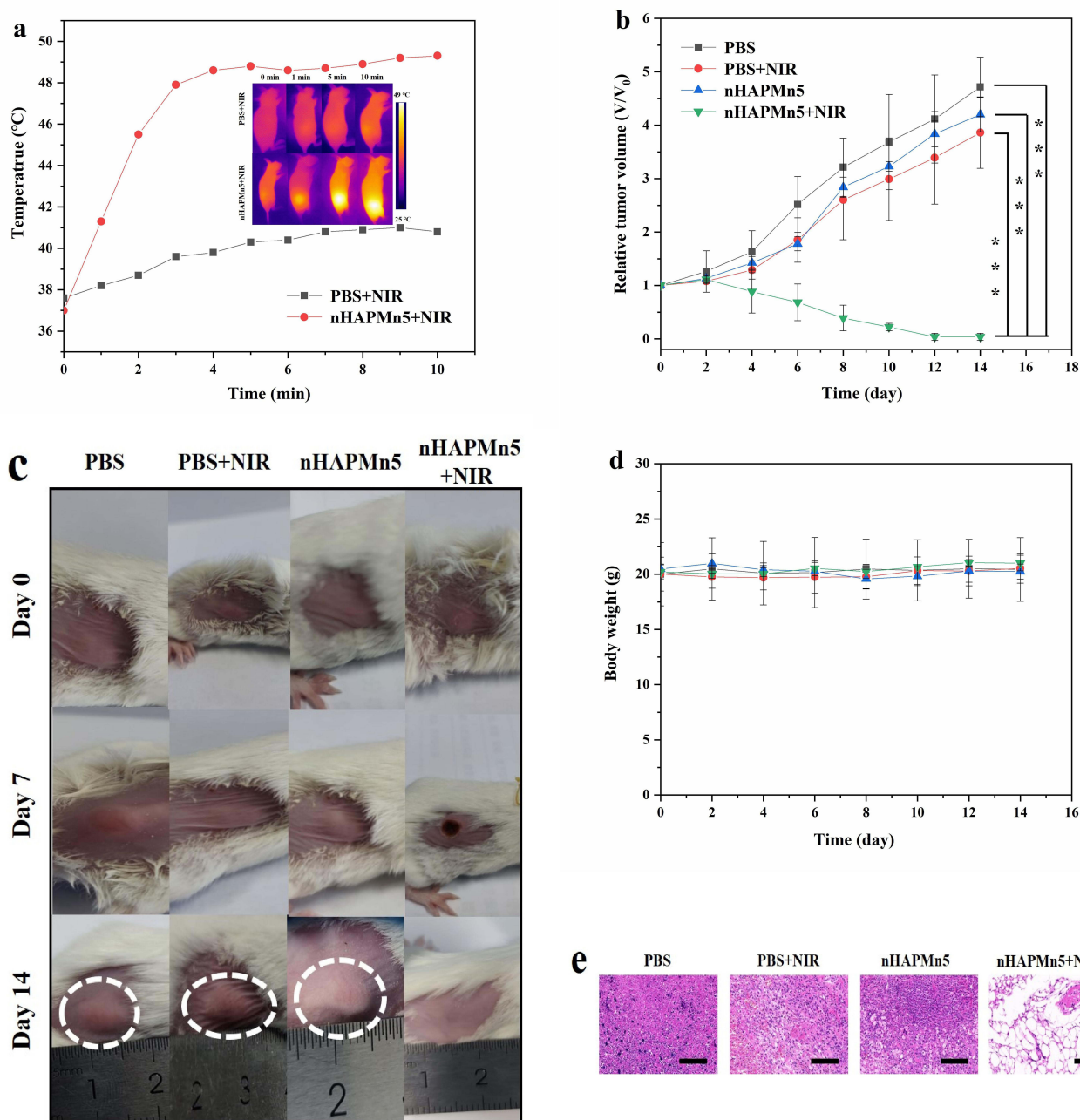


**Figure 15** (a) Temperature rise curve in the irradiated area of tumor-bearing mice injected with PBS and nHAPMn5 (10 min, 1 W/cm<sup>2</sup>, the inset corresponds to the infrared thermogram), (b) changes in the relative tumor volume of each group of tumor-bearing mice, and (c) images of tumor changes in mice before and after treatment. (d) Weight of mice within 14 days, and (e) images of tumor tissues in the above four groups analyzed by hematoxylin-eosin staining (H&E, scale bar=100  $\mu$ m).

PBS alone showed relatively small areas of apoptosis. Moreover, the tumor tissues in the PBS, PBS+NIR, and nHAPMn5 groups were dense and rich in the vascular system, indicating that the tumor grew rapidly. In summary, the tumor-bearing mice experiment showed that nHAPMn is a very promising MRI-guided PTT material, which can be used to effectively ablate tumors.

The toxicity of nHAPMn5 NP was further studied, and the blood and main organs of tumor-bearing mice were collected for routine blood parameters, blood biochemistry, and H&E staining. In the blood biochemical test, six important indexes of liver and kidney function, including aspartate ALP, transaminase (AST), alanine albumin (ALB), aminotransferase (ALT), creatinine (CREA), and BUN, were studied, and the results are shown in Figures 16a–d. No significant difference was observed in the levels of these markers between the PBS and nHAPMn5+NIR groups,

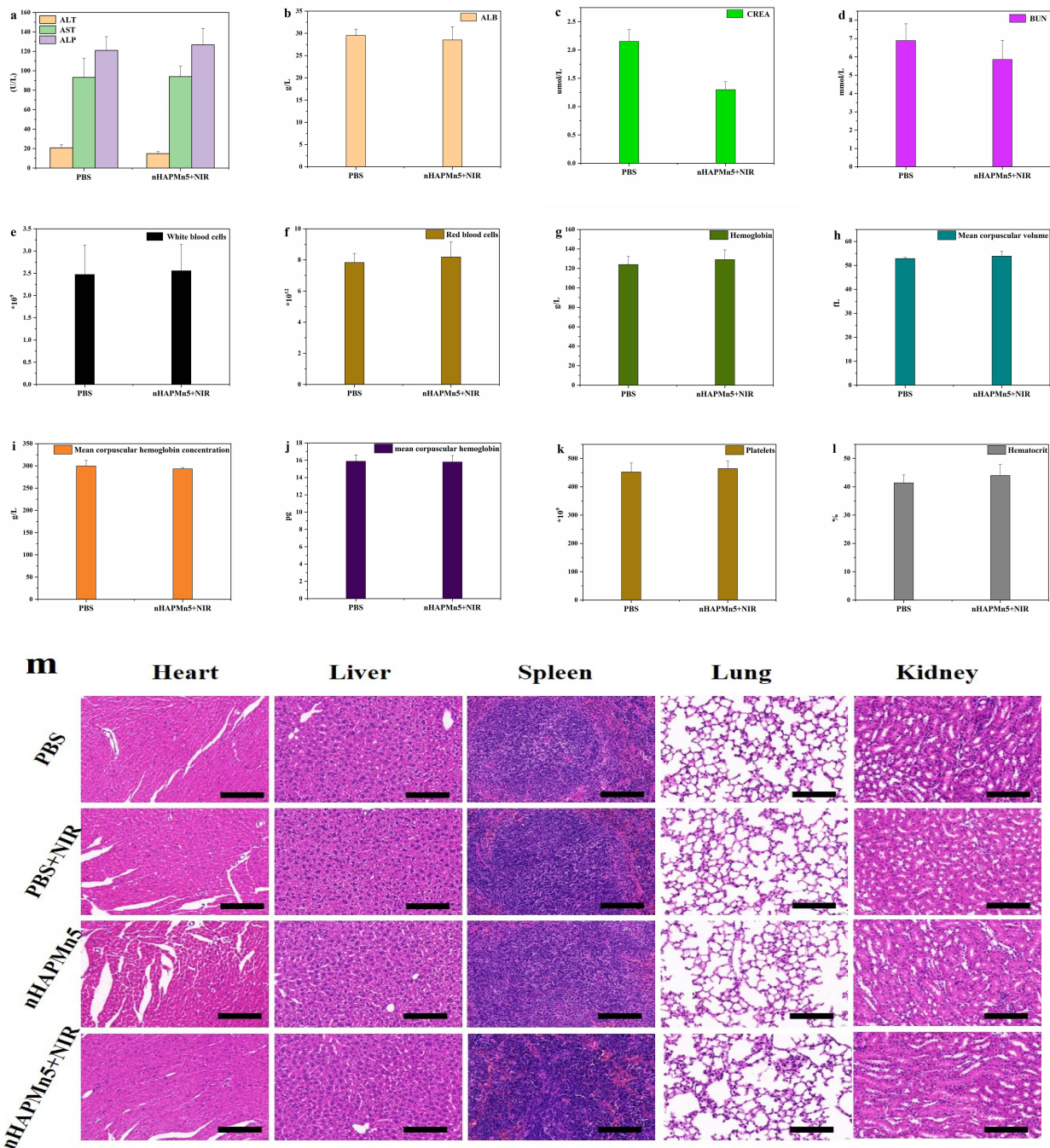


**Figure 16** (a and b) Liver function (ALT, AST, alkaline phosphatase (ALP), and ALB) and (c and d) kidney function (CREA and blood urea nitrogen (BUN)) of tumor-bearing mice. (e–l) Data of complete blood counts: white blood cells (WBCs), red blood cells (RBCs), HGB, mean corpuscular volume (MCV), mean corpuscular hemoglobin concentration (MCHC), mean corpuscular hemoglobin (MCH), PLT, and HCT. (m) H&E staining images of the primary organs 14 days after the injection of nHAPMn5 (scale bars: 100  $\mu$ m).

indicating that nHAPMn exhibits good liver and kidney safety.<sup>54</sup> Furthermore, no significant differences were observed in the standard blood parameters, including RBCs, WBCs, hemoglobin (HGB), platelets (PLT), hematocrit (HCT), MCV, MCH, and MCHC, between the PBS and nHAPMn5 groups. Such a finding indicates that nHAPMn exhibits good blood compatibility (Figures 16e–l). H&E staining was performed for further evaluation, and the result is shown in Figure 16m. Compared with the PBS group, the tissue structure of the main organs (heart, liver, spleen, lung, and kidney) of tumor-bearing mice was stained with hematoxylin and eosin, and the results show that after 14 days of PTT treatment, no

obvious damage could be observed (including inflammation, cell necrosis, or apoptosis). To study the effect of the material in the first few days, blood biochemical tests and H&E staining were also conducted 24 h and 72 h after injection, respectively (Figure S9). All the results showed that nHAPMn was safe for mice, exhibiting good MRI-guided PTT ability, biocompatibility, and negligible toxicity. The innovation of this study has been summarized in the Methods section of the [Supplementary Information](#).

## Conclusions

For the first time, Mn-doped nHAP NPs were successfully prepared for MRI-guided PTT as theranostic agents. The obtained nHAPMn NPs were well suited to MRI and showed high photothermal efficiency and negligible toxicity. In vivo MRI results showed that nHAPMn began to spread and extended over the entire tumor area 12 h after injection. In addition, nHAPMn was proven to be a potential photothermal agent with high photothermal conversion efficiency (26%) owing to its strong light absorption in the NIR range. In vivo PTT results showed that the tumor was effectively ablated within 14 days. Furthermore, our study revealed that the biodegradation of nHAPMn and the release of Mn ions amplified the MRI signals in the acidic TME, indicating that nHAPMn has good pH-responsive MR capacity in solid tumors. No recurrence or adverse effects were observed during the experiments. Therefore, nHAPMn NPs were proven to be efficient nanotherapeutic agents exhibiting great clinical benefits and transformation potential for accurate and personalized treatment of cancer.

## Acknowledgments

This research was supported by the National Natural Science Foundation of China (51672206) and the Fundamental Research Funds for the Central Universities (WUT: 2022IVB003).

## Disclosure

The authors report no conflicts of interest in this work.

## References

1. Liang S, Liao G, Zhu W, Zhang L. Manganese-based hollow nanoplatforms for MR imaging-guided cancer therapies. *Biomater Res*. 2022;26(1):32. doi:10.1186/s40824-022-00275-5
2. Xiao S, Yu X, Zhang L, et al. Synthesis of PEG-Coated, ultrasmall, manganese-doped iron oxide nanoparticles with high relaxivity for T1/T2 dual-contrast magnetic resonance imaging. *Int J Nanomed*. 2019;14:8499–8507. doi:10.2147/IJN.S219749
3. Gu X, Shu T, Deng W, Shen C, Wu Y. An X-ray activatable gold nanorod encapsulated liposome delivery system for mitochondria-targeted photodynamic therapy (PDT). *J Mater Chem B*. 2023;11(20):4539–4547. doi:10.1039/D3TB00608E
4. Xiao J, Cheng L, Fang T, et al. Nanoparticle-embedded electrospun fiber-covered stent to assist intraluminal photodynamic treatment of oesophageal cancer. *Small*. 2019;15(49):e1904979. doi:10.1002/sml.201904979
5. Wang H, An L, Tao C, et al. A smart theranostic platform for photoacoustic and magnetic resonance dual-imaging-guided photothermal-enhanced chemodynamic therapy. *Nanoscale*. 2020;12(8):5139–5150. doi:10.1039/C9NR10039C
6. Kim J, Cho HR, Jeon H, et al. Continuous O<sub>2</sub>-Evolving MnFe<sub>2</sub>O<sub>4</sub> nanoparticle-anchored mesoporous silica nanoparticles for efficient photodynamic therapy in hypoxic cancer. *J Am Chem Soc*. 2017;139(32):10992–10995. doi:10.1021/jacs.7b05559
7. Chen Q, Feng L, Liu J, et al. Intelligent Albumin-MnO<sub>2</sub> Nanoparticles as pH-/H<sub>2</sub>O<sub>2</sub>-responsive dissociable nanocarriers to modulate tumor hypoxia for effective combination therapy. *Adv Mater*. 2016;28(33):7129–7136. doi:10.1002/adma.201601902
8. Lin T, Zhao X, Zhao S, et al. O<sub>2</sub>-Generating MnO<sub>2</sub> nanoparticles for enhanced photodynamic therapy of bladder cancer by ameliorating hypoxia. *Theranostics*. 2018;8(4):990–1004. doi:10.7150/thno.22465
9. Ding B, Zheng P, Ma PA, Lin J. Manganese oxide nanomaterials: synthesis, properties, and theranostic applications. *Adv Mater*. 2020;32(10):e1905823. doi:10.1002/adma.201905823
10. Guo L, Xin H, Luo X, Zhang C. Phase evolution, mechanical properties and MRI contrast behavior of GdPO<sub>4</sub> doped hydroxyapatite for dental applications. *Mater Sci Eng C Mater Biol Appl*. 2020;111:110858. doi:10.1016/j.msec.2020.110858
11. Tao Q, He G, Ye S, et al. Mn doped Prussian blue nanoparticles for T(1)/T(2) MR imaging, PA imaging and Fenton reaction enhanced mild temperature photothermal therapy of tumor. *J Nanobiotechnology*. 2022;20(1):18. doi:10.1186/s12951-021-01235-2
12. Zhang HL, Wang Y, Tang Q, Ren B, Yang SP, Liu JG. A mesoporous MnO<sub>2</sub>-based nanoplatform with near infrared light-controlled nitric oxide delivery and tumor microenvironment modulation for enhanced antitumor therapy. *J Inorg Biochem*. 2023;241:112133. doi:10.1016/j.jinorgbio.2023.112133
13. Xie J, Yan C, Yan Y, et al. Multi-modal Mn-Zn ferrite nanocrystals for magnetically-induced cancer targeted hyperthermia: a comparison of passive and active targeting effects. *Nanoscale*. 2016;8(38):16902–16915. doi:10.1039/C6NR03916B
14. Chen Y, Li H, Deng Y, Sun H, Ke X, Ci T. Ci, near-infrared light triggered drug delivery system for higher efficacy of combined chemo-photothermal treatment. *Acta Biomater*. 2017;51:374–392. doi:10.1016/j.actbio.2016.12.004

15. Feng Q, Zhang Y, Zhang W, et al. Tumor-targeted and multi-stimuli responsive drug delivery system for near-infrared light induced chemo-phototherapy and photoacoustic tomography. *Acta Biomater.* 2016;38:129–142. doi:10.1016/j.actbio.2016.04.024
16. Sun J, Xu W, Li L, et al. Ultrasmall endogenous biopolymer nanoparticles for magnetic resonance/photoacoustic dual-modal imaging-guided photothermal therapy. *Nanoscale.* 2018;10(22):10584–10595. doi:10.1039/C8NR01215F
17. Ji H, Zhang Z, Xu J, Tanabe S, Chen D, Xie RJ. Advance in red-emitting  $Mn_4^{+}$ -Activated oxyfluoride phosphors. *J Inorg Mater.* 2020;35(8):554. doi:10.15541/jim20190554
18. Khan MM, Harunsani MH, Tan AL, Hojamberdiev M, Azamay S, Ahmad N. Antibacterial activities of zinc oxide and Mn-Doped zinc oxide synthesized using melastoma malabathricum (L.) Leaf Extract. *Bioprocess Biosyst Eng.* 2020;43(8):1499–1508. doi:10.1007/s00449-020-02343-3
19. Sinusaite L, Popov A, Raudonyte-Svirbutaviciene E, Yang JC, Kareiva A, Zarkov A. Effect of Mn doping on hydrolysis of low-temperature synthesized metastable alpha-tricalcium phosphate. *Ceram Int.* 2021;47(9):12078–12083. doi:10.1016/j.ceramint.2021.01.052
20. Chlala D, Griboval-Constant A, Nuns N, Giraudon JM, Labaki M, Lamonier JF. Effect of Mn loading onto hydroxyapatite supported Mn catalysts for toluene removal: contribution of PCA assisted ToF-SIMS. *Catal Today.* 2018;307:41–47. doi:10.1016/j.cattod.2017.04.018
21. Wang M, Li M, Wang Y, Shao Y, Zhu Y, Yang S. Efficient antibacterial activity of hydroxyapatite through ROS generation motivated by trace Mn(III) Coupled H Vacancies. *J Mater Chem B.* 2021;9(15):3401–3411. doi:10.1039/D1TB00098E
22. Ma W, Zhang H, Li S, et al. A multifunctional nanoplatfrom based on Fenton-like and Russell reactions of Cu, Mn bimetallic ions synergistically enhanced ROS stress for improved chemodynamic therapy. *ACS Biomater Sci Eng.* 2022;8(3):1354–1366. doi:10.1021/acsbomaterials.1c01605
23. Cai X, Zhu Q, Zeng Y, Zeng Q, Chen X, Zhan Y. Manganese oxide nanoparticles as MRI contrast agents in tumor multimodal imaging and therapy. *Int J Nanomed.* 2019;14:8321–8344. doi:10.2147/IJN.S218085
24. He T, Qin X, Jiang C, et al. Tumor pH-Responsive metastable-phase manganese sulfide nanotheranostics for traceable hydrogen sulfide gas therapy primed chemodynamic therapy. *Theranostics.* 2020;10(6):2453–2462. doi:10.7150/thno.42981
25. Lala S, Ghosh M, Das PK, Kar T, Pradhan SK. Mechanical preparation of nanocrystalline biocompatible single-phase Mn-Doped A-Type Carbonated Hydroxyapatite (A-cHA): effect of Mn Doping on Microstructure. *Dalton Trans.* 2015;44(46):20087–20097. doi:10.1039/C5DT03398E
26. Evis Z. Microstructural Investigation of  $Cu_2^{+}$  Doped Nanohydroxyapatites. *Mater Sci Technol.* 2013;26(5):630–632. doi:10.1179/174328409X428909
27. Ravindranadh K, Babu B, Manjari VP, Rao GT, Rao MC, Ravikumar RVSSN. Optical and structural properties of undoped and  $Mn_2^{+}$  Doped Ca–Li hydroxyapatite nanopowders using mechanochemical synthesis. *J Lumin.* 2015;159:119–127. doi:10.1016/j.jlumin.2014.10.039
28. Chen F, Huang P, Zhu YJ, Wu J, Zhang CL, Cui DX. The photoluminescence, drug delivery and imaging properties of multifunctional  $Eu_3^{+}/Gd_3^{+}$  dual-doped hydroxyapatite nanorods. *Biomaterials.* 2011;32(34):9031–9039. doi:10.1016/j.biomaterials.2011.08.032
29. Xie W, Guo Z, Gao Q, et al. Manganese-doped layered double hydroxide: a biodegradable theranostic nanoplatfrom with tumor microenvironment response for magnetic resonance imaging-guided photothermal therapy. *ACS Appl Bio Mater.* 2020;3(9):5845–5855. doi:10.1021/acsbm.0c00564
30. Zhang J, Liang C, Wei Z, et al. TME-Triggered  $MnSiO_3$ @Met@GOx Nanosystem for ATP Dual-Inhibited Starvation/Chemodynamic Synergistic Therapy. *Biomaterials.* 2022;287:121682. doi:10.1016/j.biomaterials.2022.121682
31. Shurtakova DV, Grishin PO, Gafurov MR, Mamin GV. Using DFT to calculate the parameters of the crystal field in  $Mn_2^{+}$  doped hydroxyapatite crystals. *Crystals.* 2021;11(9):1050. doi:10.3390/cryst11091050
32. Paluszkiwicz C, Ślósarczyk A, Pijoch D, et al. Synthesis, structural properties and thermal stability of Mn-doped hydroxyapatite. *J Mol Struct.* 2010;976(1–3):301–309. doi:10.1016/j.molstruc.2010.04.001
33. Webster TJ, Massa-Schlueter EA, Smith JL, Slamovich EB. Osteoblast response to hydroxyapatite doped with divalent and trivalent cations. *Biomaterials.* 2004;25(11):2111–2121. doi:10.1016/j.biomaterials.2003.09.001
34. Kandori K, Murata R, Yamaguchi Y, Yoshioka A. Protein adsorption behaviors onto Mn(II)-doped calcium hydroxyapatite particles with different morphologies. *Colloids Surf B Biointerfaces.* 2018;167:36–43. doi:10.1016/j.colsurfb.2018.03.043
35. Van HN, Tam PD, Kien NDT, Huy PT, Pham VH. Enhancing the Luminescence of  $Eu(3^{+})/Eu(2^{+})$  Ion-doped hydroxyapatite by fluoridation and thermal annealing. *Luminescence.* 2017;32(5):817–823. doi:10.1002/bio.3257
36. Wang J, Kong W, Jin H, et al. Tumor microenvironment responsive theranostic agent for enhanced chemo/chemodynamic/photothermal therapy. *Colloids Surf B Biointerfaces.* 2022;218:112750. doi:10.1016/j.colsurfb.2022.112750
37. Qi C, He J, Fu LH, et al. Huang, tumor-specific activatable nanocarriers with gas-generation and signal amplification capabilities for tumor theranostics. *ACS Nano.* 2021;15(1):1627–1639. doi:10.1021/acsnano.0c09223
38. Pina S, Canadas RF, Jiménez G, et al. Biofunctional ionic-doped calcium phosphates: silk fibroin composites for bone tissue engineering scaffolding. *Cells Tissues Organs.* 2017;204(3–4):150–163. doi:10.1159/000469703
39. Türk S, Altınsoy I, Efe GÇ, Ipek M, Özacar M, Bindal C. Biomimetic synthesis of ag, zn or co doped HA and Coating of Ag, Zn or Co Doped HA/ fMWCNT composite on functionalized Ti. *Mater Sci Eng C Mater Biol Appl.* 2019;99:986–998. doi:10.1016/j.msec.2019.02.025
40. Frangville C, Li Y, Billotey C, et al. Assembly of double-hydrophilic block copolymers triggered by gadolinium ions: new colloidal MRI contrast agents. *Nano Lett.* 2016;16(7):4069–4073. doi:10.1021/acs.nanolett.6b00664
41. Liu H, Cui X, Lu X, Liu X, Zhang L, Chan TS. Mechanism of Mn incorporation into hydroxyapatite: insights from SR-XRD, Raman, XAS, and DFT Calculation. *Chem Geol.* 2021;579:120354. doi:10.1016/j.chemgeo.2021.120354
42. Zhou Q, Dolgov L, Srivastava AM, et al.  $Mn_2^{+}$  and  $Mn_4^{+}$  red phosphors: synthesis, luminescence and applications in WLEDs. A review. *J Mater Chem C.* 2018;6(11):2652–2671. doi:10.1039/C8TC00251G
43. Van HN, Tam PD, Pham VH. Red and yellow luminescence of  $Eu_3^{+}/Dy_3^{+}$  Co-Doped Hydroxyapatite/ $\beta$ -tricalcium phosphate single phosphors synthesized using coprecipitation method. *J Appl Spectrosc.* 2018;85(4):738–742. doi:10.1007/s10812-018-0713-6
44. Dong L, Zhu Z, Qiu Y, Zhao J. Removal of lead from aqueous solution by hydroxyapatite/manganese dioxide composite. *Front Environ Sci Eng.* 2014;10(1):28–36. doi:10.1007/s11783-014-0722-5
45. Chen Z, Li Z, Li C, et al. Manganese-containing polydopamine nanoparticles as theranostic agents for magnetic resonance imaging and photothermal/chemodynamic combined ferroptosis therapy treating gastric cancer. *Drug Deliv.* 2022;29(1):1201–1211. doi:10.1080/10717544.2022.2059124
46. Su Q, Liu C, Zhu J, et al. Albumin-stabilized manganese oxide/semiconducting polymer nanocomposites for photothermal-chemodynamic therapy of hepatic carcinoma. *Front Bioeng Biotechnol.* 2022;10:919235. doi:10.3389/fbioe.2022.919235
47. Sun S, Wu D, Zhang J, Fan M, Zeng L. Manganese-doped gold nanoclusters with ultrasmall size and microenvironment-responsive visualized theranostics of tumor. *Sci Sin Chim.* 2021;51(9):1259–1268. doi:10.1360/SSC-2021-0122

48. An D, Wu X, Gong Y, et al. Manganese-Functionalized MXene theranostic nanoplatform for MRI-guided synergetic photothermal/chemodynamic therapy of cancer. *Nanophotonics*. 2022;11(22):5177–5188. doi:10.1515/nanoph-2022-0533
49. Zhao Y, Liu Y, Wang Y, et al. Rapidly clearable MnCo<sub>2</sub>O<sub>4</sub>@PAA as novel nanotheranostic agents for T<sub>1</sub>/T<sub>2</sub> bimodal MRI imaging-guided photothermal therapy. *Nanoscale*. 2021;13(38):16251–16257. doi:10.1039/D1NR04067G
50. Duan J, Liao T, Xu X, Liu Y, Kuang Y, Li C. Metal-polyphenol nanodots loaded hollow MnO(2) nanoparticles with a “dynamic protection” property for enhanced cancer chemodynamic therapy. *J Colloid Interface Sci*. 2023;634:836–851. doi:10.1016/j.jcis.2022.12.088
51. Liu Y, Gao J, Li H, et al. A near-infrared and lysosome-targeted BODIPY photosensitizer for photodynamic and photothermal synergistic therapy. *Org Biomol Chem*. 2023;21:4672–4682. doi:10.1039/D3OB00465A
52. Lin X, Zhu R, Hong Z, et al. GSH-responsive radiosensitizers with deep penetration ability for multimodal imaging-guided synergistic radio-chemodynamic cancer therapy. *Adv Funct Mater*. 2021;31(24):2101278. doi:10.1002/adfm.202101278
53. Sun R, Ge Y, Liu H, He P, Song W, Zhang X. Erythrocyte membrane-encapsulated glucose oxidase and manganese/ferrite nanocomposite as a biomimetic “all in one” nanoplatform for cancer therapy. *ACS Appl Bio Mater*. 2021;4(1):701–710. doi:10.1021/acsabm.0c01226
54. Lu N, Huang P, Fan W, et al. Tri-stimuli-responsive biodegradable theranostics for mild hyperthermia enhanced chemotherapy. *Biomaterials*. 2017;126:39–48. doi:10.1016/j.biomaterials.2017.02.025

International Journal of Nanomedicine

Dovepress

## Publish your work in this journal

The International Journal of Nanomedicine is an international, peer-reviewed journal focusing on the application of nanotechnology in diagnostics, therapeutics, and drug delivery systems throughout the biomedical field. This journal is indexed on PubMed Central, MedLine, CAS, SciSearch®, Current Contents®/Clinical Medicine, Journal Citation Reports/Science Edition, EMBase, Scopus and the Elsevier Bibliographic databases. The manuscript management system is completely online and includes a very quick and fair peer-review system, which is all easy to use. Visit <http://www.dovepress.com/testimonials.php> to read real quotes from published authors.

Submit your manuscript here: <https://www.dovepress.com/international-journal-of-nanomedicine-journal>